Advanced Functional Materials

ADVANCED FUNCTIONAL MATERIALS
www.afm-journal.de

RESEARCH ARTICLE

Manipulation of Topological Antiskyrmion Lattice Transition at Room Temperature

Zhidong He[1,2] | Zhan Wang[1,2] | Zhuolin Li[1,2] | Yunxiang Yang[1,3] | Shouguo Wang[3] | Jun Shen[4] | Tongyun Zhao[1,2] | Jianwang Cai[1,2] | Yuan Yao[1] | Jingyan Zhang[5] | Ying Zhang[1,2] | Bao-gen Shen[1,2,6]

[1]Beijing National Laboratory for Condensed Matter Physics, Institute of Physics, Chinese Academy of Sciences, Beijing, China | [2]School of Physical Sciences, University of Chinese Academy of Sciences, Beijing, China | [3]Anhui Provincial Key Laboratory of Magnetic Functional Materials and Devices, School of Materials Science and Engineering, Anhui University, Hefei, China | [4]Department of Energy and Power Engineering, School of Mechanical Engineering, Beijing Institute of Technology, Beijing, China | [5]Key Laboratory of Advanced Materials and Devices for Post-Moore Chips, School of Materials Science and Engineering, University of Science and Technology Beijing, Beijing, China | [6]Ningbo Institute of Materials Technology & Engineering, Chinese Academy of Sciences, Ningbo, Zhejiang, China

Correspondence: Jingyan Zhang (jyzhang@ustb.edu.cn) | Ying Zhang (zhangy@iphy.ac.cn)

Received: 17 November 2025 | **Revised:** 15 January 2026 | **Accepted:** 14 February 2026

Keywords: antiskyrmion configuration change | antiskyrmion lattice transition | chiral magnet $Mn_{1.4}PtSn$ | L-TEM | magnetic field manipulation

ABSTRACT

Skyrmion systems have been regarded as potential candidates for versatile energy-efficient information processing due to the intrinsic topological properties. In emerging skyrmion-based reservoir computing concepts, history-dependent spin state evolution constitutes a key physical ingredient, highlighting the importance of controllable collective dynamics in response to external stimuli. Antiskyrmions, as antiparticles of skyrmions, are expected to offer additional configurational degrees of freedom and enhanced thermal stability. However, experimental visualization of their field-dependent collective evolution remains scarce. Here we report a continuous, field-history-dependent antiskyrmion transition from a triangular to square lattice, accompanied by a sequence of intricate intermediate states in $Mn_{1.4}PtSn$ chiral magnet. Coordinated variations in antiskyrmion shape, size, and position are directly demonstrated, thereby offering experimentally multiple accessible degrees of freedom under controlled magnetic-field inputs. Systematic micromagnetic simulations reveal that the competition among Dzyaloshinskii–Moriya, dipolar, and Zeeman interactions governs the sequential reconfiguration of local spin textures underlying the observed lattice evolution. Our results provide a controllable and history-dependent antiskyrmion lattice platform with rich intermediate configuration states to explore multi-level information encoding and reservoir-computing applications.

1 | Introduction

Skyrmion systems [1–3] with quasiparticle nature and topological features [4] have demonstrated potential capabilities in racetrack memory [5–7], logic devices [8], and neuromorphic computing applications [9, 10]. In particular, skyrmion-based reservoir computing has emerged as highly efficient framework that exploits the intrinsic nonlinearity, high-dimensionality, and history-dependent dynamics of skyrmion ensembles [11–14]. In this scheme, complex spatial-temporal evolution of skyrmions serves as a core physical reservoir that maps input stimuli into a high-dimensional state, while task-specific information is extracted through a trainable readout [13, 14]. Consequently, complex pattern recognition and handwritten digit recognition have been experimentally achieved by taking advantages of the inherent dynamic skyrmion evolution within complex configurations [13]. Task-adaptive control of skyrmion reservoir properties via using spectra [15, 16] has been realized in chiral magnets

Cu_2OSeO_3, $Co_{8.5}Zn_{8.5}Mn_3$, and FeGe. These results highlight the feasibility and energy efficiency of using skyrmion-based domain evolution with high degrees of freedom in neuromorphic computing.

Following this skyrmion reservoir computing framework [14], antiskyrmions as topological counterparts of skyrmions in materials with anisotropic Dzyaloshinskii–Moriya interactions (DMI) have been proposed as promising candidates to enrich such computational paradigms owing to their additional configurational degrees of freedom and enhanced thermal stability [3, 17, 18]. Previous studies on triangular antiskyrmion lattice and configuration manipulation in chiral magnet $Mn_{1.4}Pt_{0.9}Pd_{0.1}Sn$ [3, 19–21] suggest the possibility of multi-level configuration states with high thermal stability up to 375 K. However, the experimental insight into the collective evolution of antiskyrmions under external stimuli, which constitutes a key physical prerequisite for reservoir computing and multi-level information encoding, remains limited.

In contrast to skyrmions with a single chirality of either Bloch or Néel magnetization rotation, the antiskyrmion configuration is composed of continuously alternating Bloch and Néel-type domain wall segments, as shown in the schematic (Figure 1a). Theoretically, no magnetic charge is generated and less dipole energy is consumed for Bloch-type domain walls in comparison with the Néel type, which provides an additional degree of freedom for shape and size modulation under external stimuli [22, 23]. Subsequent experiments intermittently detected a square antiskyrmion lattice in this identical magnetic material [24], yet the intrinsic correlation between triangular and square antiskyrmion lattices, as well as the nature of possible intermediate configurations, remains unexplored.

The periodic organization of atoms and spin states into lattices with defined symmetry plays a central role in determining collective physical properties. Symmetric array of nano-magnets in artificial spin ice with eight distinguished states via transport measurements has demonstrated promising application for multi-bit data storage and neuromorphic computing [25]. The ability to control intermediate configuration states through nonlinear transformations is regarded critical for enhancing the storage capacity and expanding the effective dimensions, which underpins reservoir-computing frameworks. In chiral magnets, topological skyrmion lattice transition has been demonstrated in $Co_8Zn_8Mn_4$ [26], MnSi [27], and Cu_2OSeO_3 [28] but only in reciprocal space. However, the rich degrees of freedom intrinsic to topological spin textures, such as variations in shape, size, position, and collective dynamics have not been directly captured in real space.

Lorentz transmission electron microscopy (L-TEM), with its high spatial resolution and in situ external field tunability, provides a powerful real-space approach to directly visualize nanoscale magnetic configurations and their history-dependent evolution. In this study, we directly observe the antiskyrmion transition from triangular to square lattice with complex intermediate evolution highly dependent on magnetic field history in $Mn_{1.4}PtSn$ chiral magnet. Combined experimental results and numerical micromagnetic simulations highlight the critical contributions of energy competition among external magnetic field, intrinsic anisotropic DMI, and dipolar interactions on controlling the degrees of freedom during the lattice transition. The visualization of continuous antiskyrmion lattice evolution and high degrees of freedom establish an experimentally accessible platform for exploring the collective antiskyrmion states in multi-level information encoding and reservoir-computing applications.

2 | Results and Discussion

2.1 | Generation and Characterization of Antiskyrmion Lattice

We fabricate (001) plane thin plates of $Mn_{1.4}PtSn$ [3, 29, 30] using focused ion beam (FIB) technique (Figure S1) to conduct real space observation in L-TEM. The anisotropic Dzyaloshinskii-Moriya (DM) vectors originate from intrinsic D_{2d} crystal symmetry (Figure S2), which determines the magnetic stripe domain ground state with helical propagation wavevectors along [100] and [010] axes, respectively at zero field. The antiskyrmion lattice configuration is highly dependent on magnetic field history, particularly on the contribution of in-plane magnetic fields via tilting the sample plate (Note S1). Applying a magnetic field (380 mT) at a tilting angle of 20 degrees leads to the generation of a triangular antiskyrmion lattice, in contrast to isolated antiskyrmions without in-plane field manipulation, which is consistent with previous experimental reports [3, 19]. The triangular lattice becomes slightly distorted once the angle is tilted back to 0 (removing in-plane magnetic field). Subsequently, as the magnetic field decreases, the antiskyrmion configuration transition from triangular to square lattice (schematic illustration in Figure 1b) is directly observed as shown in Figure 1c,e at room temperature.

Two bright and dark contrast regions along respective vertical and horizontal directions in L-TEM images (Figure 1c,e) originate from alternating Bloch and Néel walls within a single antiskyrmion. Further micromagnetic simulations (Figure 1d,f) and L-TEM image simulations (Figure 1g,i; Figure S3) based on the material parameters of $Mn_{1.4}PtSn$ (Methods and Note S2) confirm the consistent magnetization configuration of the antiskyrmion lattice. It is demonstrated that the shape and size of individual antiskyrmion change significantly during the transformation from triangular to square lattice while in situ reducing the magnetic field from 380 mT to zero. Corresponding schematic illustrations (Figure 1h,j) manifest multiple degrees of freedom including size, shape and configuration arrangement, where Bloch and Néel domain wall segments are marked with blue and red color, respectively. The individual antiskyrmion tends to have a larger size, square shape and a larger Bloch to Néel domain wall ratio inside the square lattice. The in-plane magnetization configuration of antiskyrmion lattice is identified via using transport-of-intensity equation (TIE) method [31] (Figure S4) based on L-TEM images at under-focus and over-focus Fresnel modes ($\Delta z = \pm 500$ μm), consistent with previous studies [24]. By repeating the experimental protocols, we conclude that the triangular-to-square lattice transition can be effectively manipulated by magnetic field.

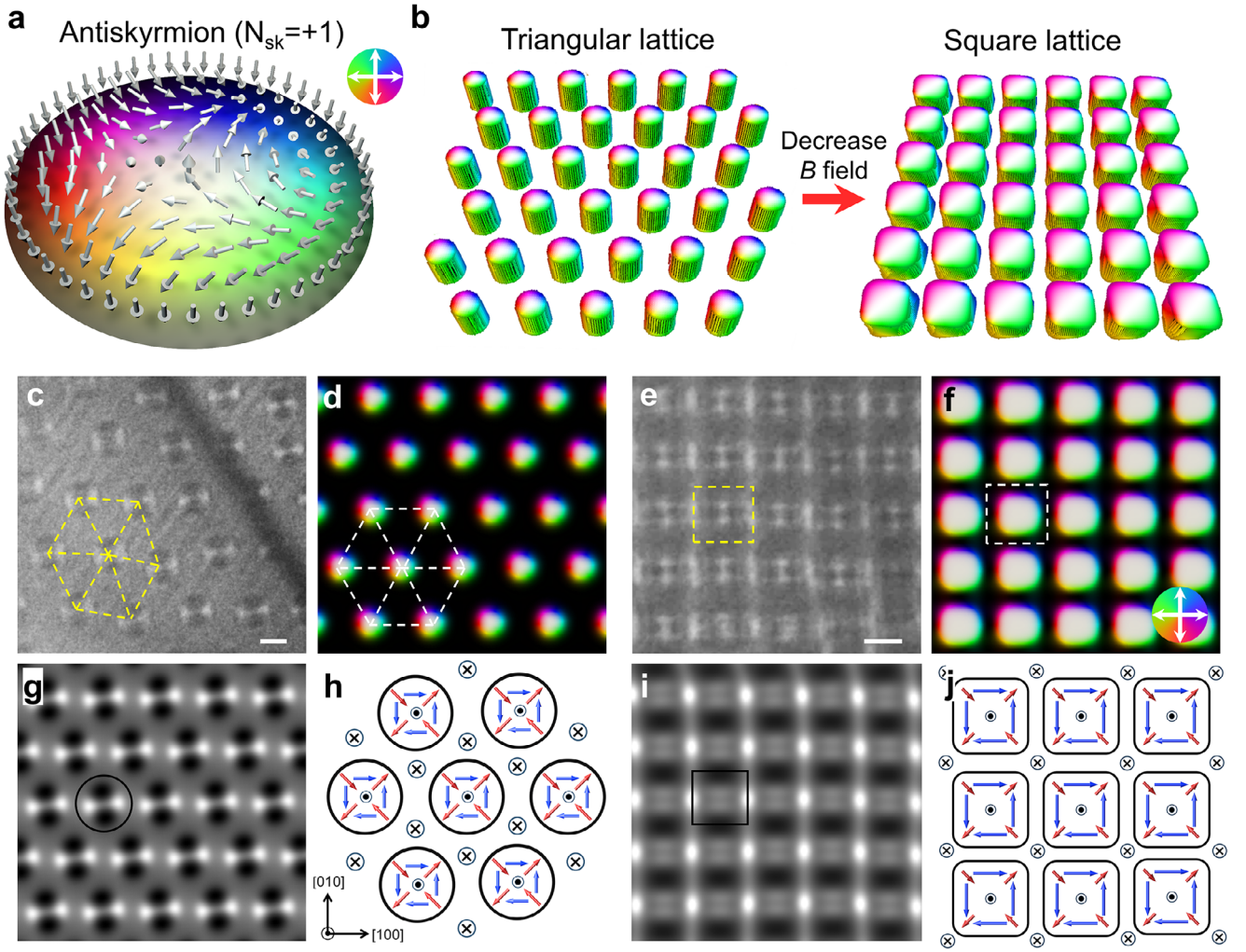

FIGURE 1 | Real-space observation of antiskyrmion transition from triangular to square lattice within (001) plane of chiral magnet $Mn_{1.4}PtSn$ at room temperature. (a) Schematic illustration of topological antiskyrmion magnetization texture with $N_{sk} = 1$. (b) Schematic of antiskyrmion lattice transition. (c–f) L-TEM images acquired at a defocus value of 500 μm, showing the representative triangular (c) and square (e) antiskyrmion lattice under perpendicular magnetic fields of 380 and 0 mT, respectively. Scale bar, 100 nm. The corresponding simulated in-plane magnetization distributions for the triangular (d) and square (f) antiskyrmion lattice with color wheels in the insets indicating magnetization orientation. (g–j) Simulated Fresnel L-TEM images of triangular (g) and square (i) antiskyrmion lattices at a defocus value of 500 μm, demonstrating the domain contrast of Bloch walls due to the Lorentz force deflection of electrons. The schematic configurations of triangular (h) and square (j) antiskyrmion lattices, well illustrating the changes in shape, size, and the ratio between Bloch and Néel wall segments. Red arrows for Néel-type magnetization along [110] and [1$\bar{1}$0] directions and blue arrows for Bloch-type magnetization along [100] and [010] directions.

2.2 | Magnetic Field and Temperature Dependency of Antiskyrmion Evolution

To better understand the dependency of the intermediate antiskyrmion evolution on magnetic field and temperature, we record a series of L-TEM images at respectively 295 and 150 K while reducing magnetic field as shown in Figure 2. Starting from the triangular lattice at 380 mT (Figure 2a), the rearrangement of antiskyrmion in response to the magnetic field is directly observed. When the magnetic field is reduced to 265 mT, the configuration change of individual antiskyrmions from circular to square shape is identified together with the lattice rearrangement (Figure 2e). It is demonstrated that the intermediate transition including individual antiskyrmions and their lattice is gradual and continuous while decreasing the magnetic field as shown in Figure 2c-e (Figure S5).

The decrease of magnetic field enables the peripheral magnetic moment to rotate away from the magnetic field direction to in-plane direction, resulting in enlargement of antiskyrmion size. The square lattice appears densely packed (Figure 2f) when the magnetic field is reduced to 247 mT and remains robust at zero field (Figure 2h). Occasional appearance of helical domains as localized topological defects inside the square lattice enriches the domain states. We demonstrate that the magnetic field-dependent lattice transition can be extended over a wide temperature range down to 150 K (Figures 2i-l), below which stripe domains substitute the lattice due to the spin reorientation transition. It should be noted that circular and square

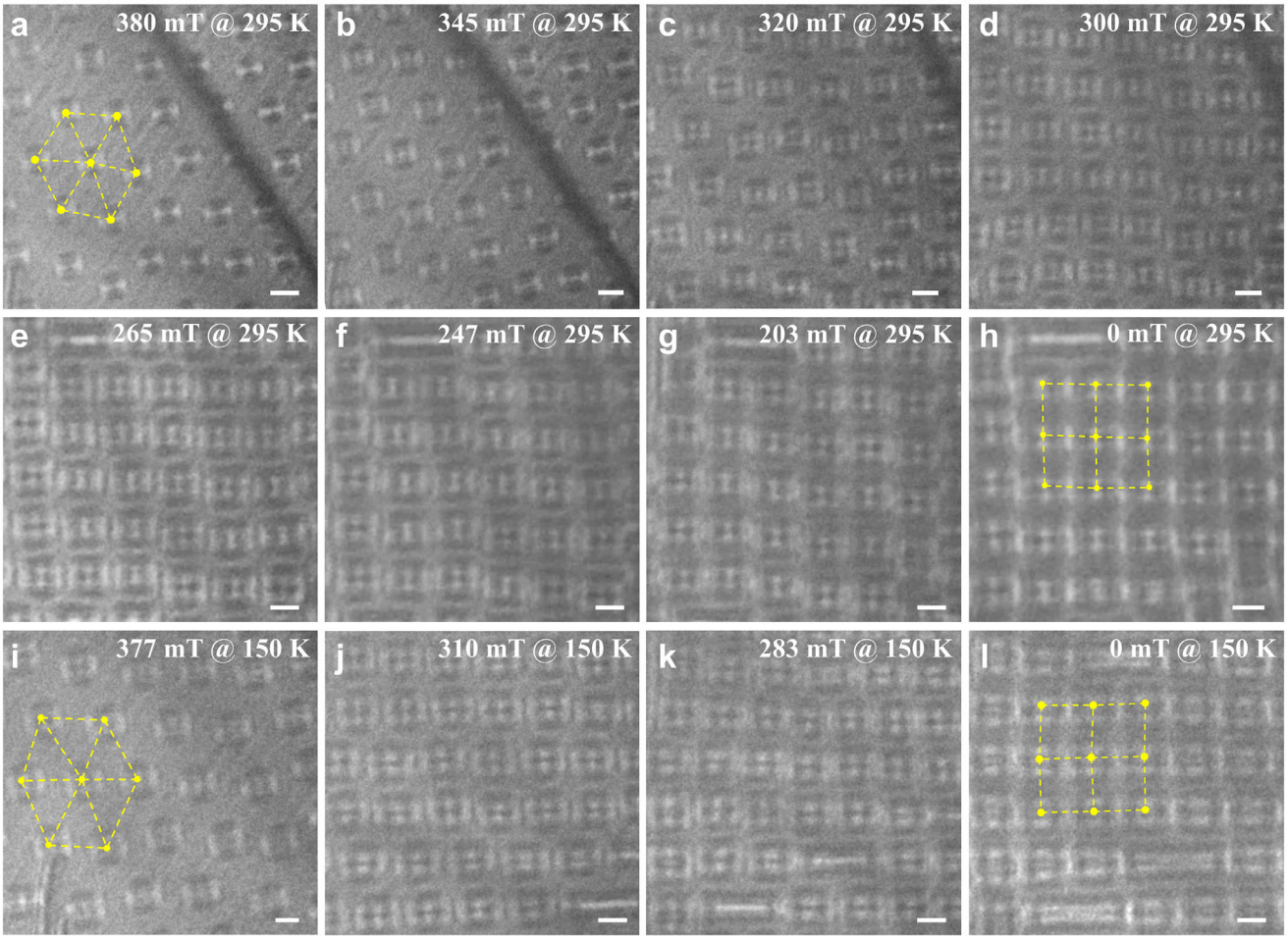

FIGURE 2 | Complex antiskyrmion lattice evolution at different magnetic fields and temperatures in (001) thin plate of $Mn_{1.4}PtSn$. (a–l) Representative under-focus L-TEM images showing continuous evolution from an antiskyrmion triangular to a densely packed square lattice while decreasing magnetic fields at 295 K (a–h) and 150 K (i–l). The antiskyrmion triangular lattice (a) is generated from the ground-state helical stripe domain at 380 mT. While decreasing the magnetic fields, the shape of antiskyrmions gradually transforms from circular to square, accompanied by an increase in particle size and a decrease in nearest-neighbor antiskyrmion distance. When the magnetic field is completely removed, the square lattice (h) remains stable. Scale bar, 100 nm.

antiskyrmions share the same topological characteristics with the total topological number essentially unchanged during the transition.

2.3 | Summary of Antiskymion Configuration Change During Lattice Transition

The extracted topological lattice demonstrates the overall distribution of the nearest neighbour elements and defects in these two antiskyrmion lattices as shown in Figure 3a-d. The topological defects in the form of helical domains are observed in the square lattice, which are randomly induced during antiskyrmion rearrangement as illustrated in simulations (Figure S6). The L-TEM images focusing on a single antiskyrmion clearly depict the configuration evolution including shape, size and domain contrast at different magnetic fields, indicating larger Bloch to Néel domain wall ratio in square antiskyrmion (Figure 3e; Figures S7 and S8). The statistical plots in Figure 3f,g summarize the gradual increase in antiskyrmion size (Figure 3f) and decrease in nearest-neighbor antiskyrmion distance (Figure 3g) as decreasing the magnetic fields. We define the size of the magnetic structure based on its spatial contrast extension along the [100] crystallographic axis. To determine the effective boundary, the image contrast is normalized, and the boundary is identified as the position corresponding to 85% of the peak brightness. Further quantification of the antiskyrmion lattice evolution via using the radial distribution function (RDF) (Figure S9) confirms the conclusion of direct L-TEM observations. The coordinated trend seems qualitatively consistent with a smaller size for larger distance but no exact quantitative relationship is confirmed so far. Therefore, the changes in antiskyrmion size and nearest-neighbor antiskyrmion distance provide independent degrees of freedom in contrast to the fixed parameters within narrow temperature and field windows in skyrmion helimagnets [1, 2, 4, 32].

The intricate interplay among external magnetic fields, anisotropic DMI, and dipole-dipole interactions facilitates controlling antiskyrmion configuration through external stimuli. The applied magnetic field gradually drives the peripheral magnetization of individual antiskyrmions along the field direction, thereby shrinking and reducing the size, which is

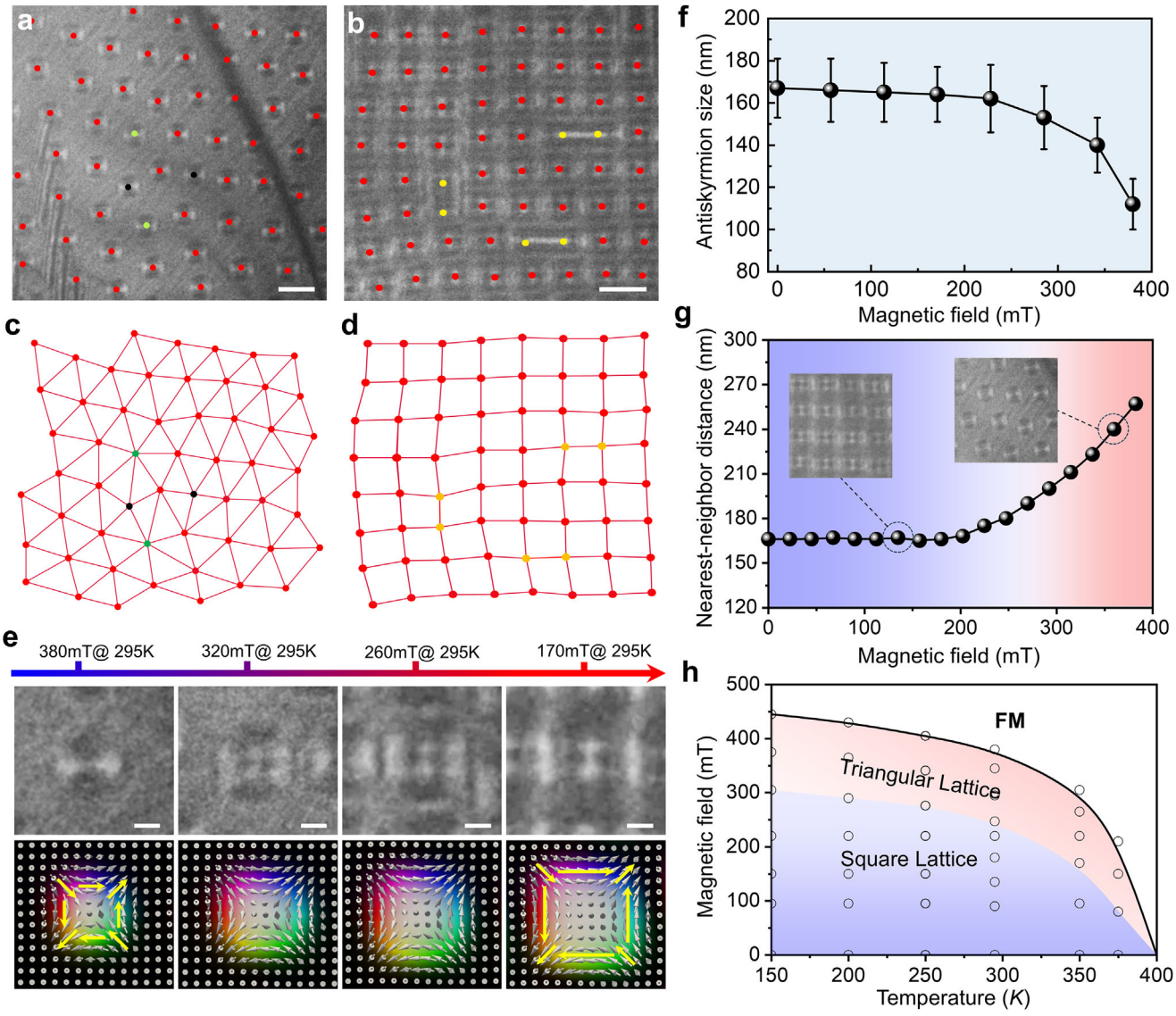

FIGURE 3 | Summary of configuration freedoms in response to external magnetic field and temperature during antiskyrmion lattice transformation. (a, b) Real space L-TEM images showing triangular and square lattices at magnetic field of 380 and 0 mT. Scale bar, 200 nm. (c, d) Extracted topological morphology from antiskyrmion lattices with six and four neighbors highlighted in red. Topological defects are marked in orange. (e) L-TEM images and corresponding micromagnetic simulations focusing on a single antiskyrmion spin texture evolution from circular to square shape while decreasing magnetic field at 295 K. Arrows and colors indicate the magnitude and direction of in-plane magnetization. The length of antiskyrmion boundary wall marked with yellow, indicating increased Bloch to Néel domain wall ratio from circular to square shape transition. Scale bar, 50 nm. (f) Dependence of antiskyrmion size on magnetic field with error bars showing the standard deviation. (g) Dependence of nearest-neighbor antiskyrmion distance on magnetic field with critical transition point marked out. (h) Summarized magnetic phase diagram for antiskyrmion lattice transition showing significant correlation with magnetic field and temperature.

theoretically and experimentally consistent with skyrmion evolution [33, 34]. The contribution of dipole–dipole interactions to the antiskyrmion configuration varies with the magnitude of input magnetic field. When the effect of magnetic field is dominated, circular antiskyrmions tend to form. Once the magnetic field decreases below a certain threshold, the expansion of the total wall region becomes significant due to the increased peripheral canted magnetization. At this stage, Bloch walls are preferred over Néel walls in minimizing magnetic energy loss, manifesting the contribution of dipole–dipole interactions. Therefore, for larger-size antiskyrmions, the region of Bloch wall expands along [100] and [010] directions, while the Néel wall contracts along [110] and [1$\bar{1}$0] directions, forming square-shape antiskyrmions. Although the total domain wall length increases from circular to square shape, the Bloch to Néel domain wall ratio takes precedence in minimizing the energy of DMI and dipole interactions.

Off-axis electron holography experiment is further conducted at in-focus state. The corresponding antiskyrmion configuration (Figure S8) confirms consistent distribution of Bloch and Néel wall segments inside antiskyrmion. Interestingly, similar phenomena have been observed in the topological helicon lattice in liquid crystal systems, where shape deformation and lattice

symmetry changes were manipulated by external electric field [35]. The H-T phase diagram based on L-TEM measurements (Figure 3h) summarizes the overall field-induced lattice transition over a broad temperature range (150–375 K), which provides more convenient manipulation option in comparison with previously reported skyrmion lattice transitions at low temperatures and following complex field-cooling processes (Table S1) [26–28].

2.4 | Micromagnetic Simulations to Reveal Complex Domain Evolution Mechanism

Micromagnetic simulations based on Landau–Lifshitz–Gilbert (LLG) equation by using MuMax3 [36] software demonstrate the dynamic origination of the antiskyrmion lattice transformation under a magnetic field (details in Methods). The magnetization distribution $\boldsymbol{m}(\mathrm{r})$ is determined by minimizing the magnetic free energy $E = \int \varepsilon \, d\boldsymbol{r}$ with energy density $\varepsilon(\mathrm{r})$ given by

$$E = \int_{V_s} \left(\varepsilon_{\mathrm{ex}} + \varepsilon_{\mathrm{dmi}} + \varepsilon_{\mathrm{anis}} + \varepsilon_{\mathrm{Zeeman}} + \varepsilon_{\mathrm{dipole}}\right) d\boldsymbol{r}$$

where the first, second, third, fourth, and fifth terms correspond to the energy density of exchange interaction, anisotropic DMI interaction, uniaxial anisotropy, Zeeman, and dipole, respectively. The real-space distribution of the local magnetic moments $\boldsymbol{m}$ (Figure 4a-d), energy density ε (Figure 4e-h), and topological charge density n_{sk} (Figure 4i-l) are respectively calculated during the antiskyrmion lattice transformation under different magnetic fields. Antiskyrmions are initially generated in a triangular lattice (Figure 4a) at a magnetic field of 350 mT, where Zeeman energy determines the energy landscape in contrast to the minor contribution of long-range dipolar interaction and isotropic energy density for large spacing (Figure 4e). When decreasing the magnetic field, the magnetic moments in peripheral antiskyrmions begin to rotate into the in-plane direction (Figure 3e), enlarging the antiskyrmion size and facilitating the antiskyrmion morphology transition from circular to square (Figure 4a-d). The short-range anisotropic interactions become dominant in theses deformed square antiskyrmion textures, leading to antiskyrmion rearrangement. The divergence of Néel-type magnetization carries magnetostatic charges $\rho_{\mathrm{mag}} \propto \nabla \cdot \boldsymbol{m}$ at four corners of the square configuration with opposite sign marked out along the [110] and [1$\bar{1}$0] axes due to the opposite chirality of anisotropic DMI.

The micromagnetic simulations clearly demonstrate the magnetostatic charge distribution and mutual force relationship in the magnified magnetization distribution (Figure 4m; Figure S10). The magnetostatic charges with opposite signs introduce attractive forces for adjacent antiskyrmions along the [100] and [010] axes (red arrows in Figure 4m), while the repulsive forces dominate along the [110] and [1$\bar{1}$0] axes (blue arrows in Figure 4m). Particularly, the increase in size and decrease in nearest-neighbor antiskyrmion distance makes the short-range anisotropic antiskyrmion interactions competitive with other interactions, resulting in triangular to square lattice transition. A perfect square lattice is obtained at about 170 mT, where an anisotropic energy density distributes at the antiskyrmion-antiskyrmion interface with slightly higher energy along [100] and [010] axes than other directions as shown in the red box area of Figure 4h. The local interactions between antiskyrmions cause the steep spatial variation of the magnetic moments (Figure S11) at the interface and disturb the ideal spin modulation pitch, leading to a larger energy cost. Consequently, additional topological charge density n_{sk} accumulates near the interface along [100] and [010] axis (red boxed area in Figure 4l) and counter-vortices are induced between the original antiskyrmions (blue boxed area in Figure 4l) with negative n_{sk}, maintaining the net total topological charge unchanged (Figure S11).

The individual energy (Figure 4n) for different interactions during the antiskyrmion lattice transition are calculated while varying the external magnetic field. It is demonstrated that the anisotropic DMI energy and dipole energy (black and red lines in Figure 4n) linearly decrease in comparison with significant increase in Zeeman energy (blue lines in Figure 4n) during the lattice transition with decreasing magnetic fields. This highlights the key role of anisotropic DMI and dipole interactions in competing with the external magnetic field to stabilize different antiskyrmion configurations and lattice structures, which is consistent with experimental results. The anisotropic DMI and dipolar interactions are critical for stabilizing square lattices of antiskyrmions in contrast to the dominant contribution of magnetocrystalline [37] and exchange anisotropy [38] for that of skyrmion lattices.

Understanding the microscopic mechanisms and critical interactions among topological units is essential for establishing well-defined and robust configuration states for exploring versatile spintronic applications. Previous studies on skyrmion-based systems have demonstrated that their collective dynamics can be electrically probed through multiple established readout channels [13, 14]. Building on this foundation, the intermediate states during antiskyrmion lattice evolution are, in principle, compatible with existing electrical detection schemes for skyrmions including magnetoresistance [39, 40], topological Hall signals [4], alternating-current susceptibility [41], and spin-wave spectroscopy [14], thereby defining feasible experimental routes for future information process. To clarify this connection at a conceptual level, a schematic illustration is provided in Figure S12, which outlines how the complex, field-history-dependent intermediate states of antiskyrmion lattices can be mapped onto a generic reservoir-computing framework.

3 | Conclusions

By conveniently manipulating the external magnetic field in L-TEM, we have directly observed the intermediate evolution of the antiskyrmion lattice transition from triangular to square in chiral magnet $Mn_{1.4}PtSn$. The individual topological antiskyrmion particles exhibit significant field-induced configuration changes in shape, size and position to compose different lattices. Micromagnetic simulations further verify the antiskyrmion lattice transition together with complex intermediate evolution, providing microscopic insight into the competing interactions that govern antiskyrmion stability and collective reorganization behaviour. The ability to control the freedom of topological units during lattice transition provides a rich platform for exploring high-efficient and multi-level information processing alternatives.

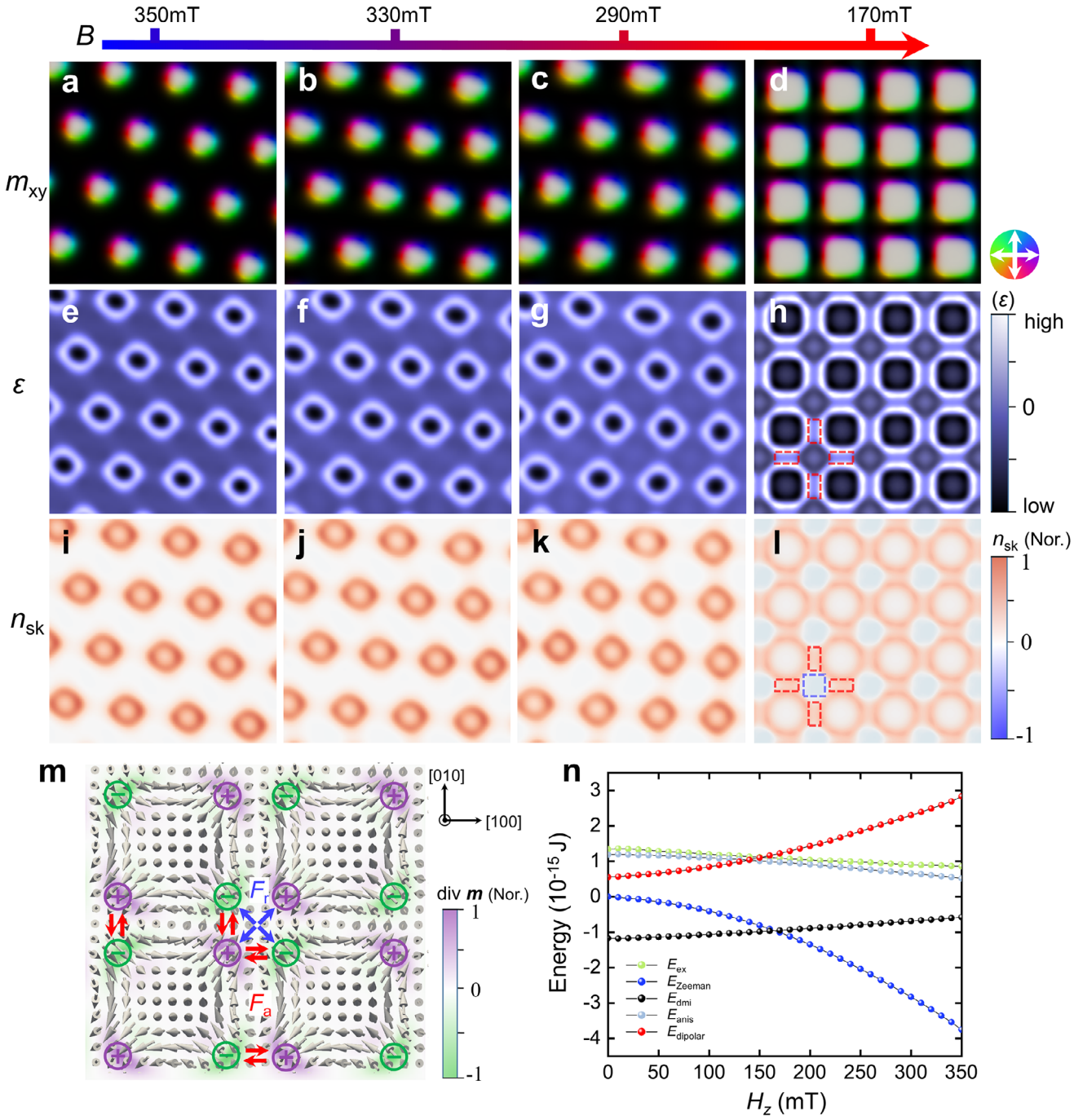

FIGURE 4 | Micromagnetic simulations to reveal the dynamic evolution and mechanism of field-induced antiskyrmion lattice transition. (a–d) Local magnetization intensity (m) distribution of antiskyrmions lattice while decreasing the magnetic field. The direction of in-plane (m_{xy}) magnetization is indexed by color wheel and the magnetization intensity along z-axis (m_z) is represented by white ($+m_z$) and black ($-m_z$) regions. (e–l) Corresponding contour plots of the energy density ε (e–h) and topological charge density n_{sk} (i–l). The non-uniform arrangement of magnetic moments accumulates additional topological charge n_{sk} (the red dashed box in l) near the interface leaving negative n_{sk} generated in the intermediate region (the blue dashed box in l) to maintain the net total topological charge. (m) Spatial distribution of magnetostatic charges based on simulated magnetization, indicating short-range anisotropic interactions between antiskyrmions. Purple and green represent opposite magnetostatic charges $\nabla \boldsymbol{m}$. Consequently, the attractive forces (F_a) marked with red arrows and repulsive forces (F_r) with blue arrows are introduced at different directions. (n) Dependency of different magnetic energy on magnetic fields, where E_{ex}, E_{Zeeman}, E_{dmi}, E_{anis}, $E_{dipolar}$ represent exchange interaction energy, Zeeman energy, anisotropic DMI interaction energy, uniaxial anisotropy energy, and dipolar energy, respectively.

4 | Methods

4.1 | Preparation of $Mn_{1.4}PtSn$ Single Crystals

The $Mn_{1.4}PtSn$ single crystal was synthesized using the flux growth method [29, 30] with Sn as a fluxing agent in a box furnace (KEJING KSL-1700X). High-purity Mn (99.999%) and Pt (99.999%) metals were combined in a molar ratio of 3:1, with a total mass of 0.75 g, and mixed with approximately 10 g of Sn. The mixture was placed into an alumina crucible, which was then sealed within a quartz tube under an argon pressure of 0.2 bar. The sealed quartz tube was heated in a box furnace at 1323 K for 24 h to ensure compositional homogeneity. Subsequently, the temperature was rapidly reduced to 923 K, followed by a slow cooling process at a rate of 0.5 K/h down to 723 K, where it was maintained for 48 h to promote better crystallization. Finally, the excess flux was removed via centrifugation.

4.2 | Fabrication of $Mn_{1.4}PtSn$ Thin Plates

$Mn_{1.4}PtSn$ thin plate with a thickness of approximately 125 nm was fabricated from bulk crystals for real-space L-TEM observation by using the lift-out method in a focused ion beam microscope (Zeiss 550 FIB), which includes a gas injection system and a micromanipulator (MM3A, Kleindiek). A cuboid with dimensions of 4 μm in length and 3 μm in width was cut from a $Mn_{1.4}PtSn$ single crystal in a Ga+ ion contained dual beam system of FIB operating at an accelerated voltage of 30 keV. PtC_x was used as an adhesive to attach the separated cuboid to the micromanipulator for subsequent mounting onto a copper grid. Under the observation of the TEM electron beam in the [001] direction, the cuboid was thinned to a thickness of approximately 125 nm. The selected-area electron diffraction (SAED) was employed to ascertain the crystalline orientation of the (001) thin plate.

4.3 | L-TEM Measurements

For the L-TEM measurements, the real space magnetic domain imaging was carried out using Lorentz Fresnel method in a JEOL L-TEM (JEOL2100F). This instrument operates at an acceleration voltage of 200 kV and enables in situ observation of the magnetic structure of the sample by leveraging the intrinsic interaction between incident electrons and the in-plane magnetic induction [42]. The L-TEM images obtained during the experiment were recorded by a charge-coupled device (CCD) camera. Based on multiple experimental observations, a defocus value of 500 μm was selected to acquire Lorentz TEM images in order to optimize the magnetic domain contrast for a sample thickness of approximately 125 nm. By adjusting the objective lens current, an external magnetic field is applied perpendicular to the sample plate and parallel to the incident electron beam. An in-plane component of the magnetic field was applied by tilting the thin plate away from the [001] axis utilizing a dual-tilt holder that permits a maximum tilt angle of up to ±30°. A Gatan dual-tilt liquid nitrogen sample holder was used to alter the sample temperature between 150 and 380K.

4.4 | Micromagnetic Simulations

For the micromagnetic simulation of the antiskyrmion lattice transition dynamics, we incorporated an anisotropic DMI and improved the numerical precision by customizing the code on the basis of the well-established GPU-accelerated MuMax3 [36] framework, which is grounded in the Landau–Lifshitz–Gilbert (LLG) equation. The energy functional is given by:

$$E = \int_{V_s} \left(\varepsilon_{ex} + \varepsilon_{dmi} + \varepsilon_{anis} + \varepsilon_{Zeeman} + \varepsilon_{dipolar}\right) d\boldsymbol{r} \quad (1)$$

where the energy density includes exchange interaction $\varepsilon_{ex} = A_{ex}((\partial_x \mathbf{m})^2 + (\partial_y \mathbf{m})^2 + (\partial_z \mathbf{m})^2)$, anisotropic DMI interaction $\varepsilon_{dmi} = D_{dmi}\left(m_z \frac{\partial m_x}{\partial x} - m_x \frac{\partial m_z}{\partial x} - m_z \frac{\partial m_y}{\partial y} + m_y \frac{\partial m_z}{\partial y}\right)$, uniaxial anisotropy $\varepsilon_{anis} = -K_u(\mathbf{u} \cdot \mathbf{m})^2$, Zeeman $\varepsilon_{Zeeman} = -\mu_0 M_s \mathbf{H}_{ext} \cdot \mathbf{m}$ with the external magnetic field $\mathbf{H}_{ext}$ and vacuum permeability μ_0, dipolar $\varepsilon_{dipolar} = -\frac{1}{2}\mu_0 M_s \boldsymbol{H}_{DI} \cdot \boldsymbol{m}$ with the dipolar field $\mathbf{H}_{DI}$. Also, $\mathbf{m} = \mathbf{m}(r)$ is a unit-vector field defining the direction of magnetization $\mathbf{M} = \mathbf{m}(r)M_s$. Furthermore, A_{ex}, D_{dmi}, K_u, M_s, are the exchange interaction, anisotropic DMI interaction, uniaxial anisotropy, saturation magnetization, respectively. In the simulation, we employed experimentally evaluated magnetic parameters based on previously reported [30] results at $T = 300$ K (Figure S13). The material parameters include the exchange interaction $A_{ex} = 9.58\times10^{-12}$ J m^{-1}, the uniaxial anisotropy $K_u = 1.25 \times 105$ J m^{-3} oriented along the [001] crystallographic axis, and the saturation magnetization $M_s = 6.37 \times 105$ A m^{-1} is incorporated, as detailed in Note S2. The anisotropic DMI is treated as a perturbation parameter, and simulations are conducted with varying DMI values of 2, 4, 6 and 8×10^{-4} J m^{-2}, respectively. The configuration obtained at $D_{dmi} = 8\times10^{-4}$ J m^{-2} exhibited the best agreement with experimental observations of the antiskyrmion lattice transition under varying magnetic fields. The system size for the simulation is set to be 600 nm × 600 nm × 600 nm and discretized into a 200 × 200 × 20 cube with periodic boundary conditions in the x–y plane. To simulate the presence of impurities, a uniaxial anisotropy $K_u = 2\times 105$ J m^{-3} is introduced at randomly chosen sites, with an impurity density of 0.12%.

4.5 | Simulation of L-TEM Images

We simulated L-TEM images for magnetic textures by calculating the corresponding magnetic phase shifts of the incident electrons [43]. The electron beam's wave function, under the phase-object approximation, is expressed as:

$$\Psi_0(x, y) \propto \exp(i\phi(x, y)) \quad (2)$$

where $\varphi(x, y)$ denotes the magnetic phase shift.

The magnetic phase variation of incident electrons arises from their interaction with the in-plane magnetizations of the magnet. The magnetic sample acts as a phase modulator for the incident electron wave, the magnetic phase variation can be calculated using:

$$\phi(x, y) = \frac{2\pi e}{h} \int_{-\infty}^{+\infty} A_z(x, y, z)\, dz \quad (3)$$

In this expression, $A_z(x,y,z)$ represents the z-component of the magnetic vector potential, where z aligns with the direction of the incident electron beam, e denotes the elementary unit of charge, and h is Planck's constant. The spin configurations were derived from the output of micromagnetic simulations. The magnetic phase shift was computed using a self-customized Python code.

Within the context of the Fresnel L-TEM mode of operation, the electron beam's wave function at the detector plane is given by:

$$\Psi_{\triangle z}(x,y) \propto \iint dx'dy'\Psi_0(x,y)K(x-x',y-y') \quad (4)$$

Here, the kernel $K(\xi, \eta)$ function follows $K(\xi,\eta) = \exp(\frac{i\pi}{\lambda\Delta z}(\xi^2+\eta^2))$, where λ represents the relativistic electron wavelength, defined as: $\lambda = \frac{hc}{\sqrt{(eU)^2+2eUm_ec^2}}$. In this equation, U is the accelerating voltage constant, m_e is the electron rest mass, Δz is the defocus value, and c is the speed of light. In the simulation, we use parameters including an acceleration voltage U of 200 kV, sample thickness t of 100 nm, and defocus value Δz of ±500 µm are used in simulation. All the aberrations of the microscope are set to zero. The intensity of the L-TEM image is obtained by performing an inverse Fourier transform based on:

$$I(x,y) \propto |\Psi_{\triangle z}(x,y)|^2 \quad (5)$$

Thus, we simulate the L-TEM images of magnetic domains accordingly, as shown in Figure S3.

Author Contributions

Y.Z. supervised the project. Z.D.H., Z.H.C., and Z.W. synthesized the $Mn_{1.4}PtSn$ bulk crystals. Z.D.H. and Y.Z. performed L-TEM observation. H.Z.D. and Z.L.L. performed the micromagnetic simulation. Z.D.H., J.W.C., J.Y.Z., and Y.Z. analyzed the experimental data and plotted the figures; Z.D.H. and Y.Z. wrote the manuscript after discussing data with J.S., S.G.W., T.Y.Z., J.W.C., J.Y.Z., and B.G.S.

Acknowledgements

We would like to thank Wuming Liu, Xiaoling Cui and Ruijuan Xiao for helpful discussion. This work was supported by the National Key R&D Program of China (Grant No. 2024YFA1611301), the National Natural Science Foundation of China (Nos. 52525108, 52271195, 52088101, 52130103), the CAS Project for Young Scientists in Basic Research (No. YSBR-084), and the Postdoctoral Fellowship Program and China Postdoctoral Science Foundation (No. BX20250164).

Conflicts of Interest

The authors declare no conflicts of interest.

Data Availability Statement

The data that support the findings of this study are available from the corresponding author upon reasonable request.

References

1. S. Mühlbauer, B. Binz, F. Jonietz, et al., "Skyrmion Lattice in a Chiral Magnet," *Science* 323 (2009): 915–919, https://doi.org/10.1126/science.1166767.

2. X. Yu, Y. Onose, N. Kanazawa, et al., "Real-Space Observation of a Two-Dimensional Skyrmion Crystal," *Nature* 465 (2010): 901–904, https://doi.org/10.1038/nature09124.

3. A. K. Nayak, V. Kumar, T. Ma, et al., "Magnetic Antiskyrmions Above Room Temperature in Tetragonal Heusler Materials," *Nature* 548 (2017): 561–566, https://doi.org/10.1038/nature23466.

4. N. Nagaosa and Y. Tokura, "Topological Properties and Dynamics of Magnetic Skyrmions," *Nature Nanotechnology* 8 (2013): 899–911, https://doi.org/10.1038/nnano.2013.243.

5. J. Iwasaki, M. Mochizuki, and N. Nagaosa, "Current-Induced Skyrmion Dynamics in Constricted Geometries," *Nature Nanotechnology* 8 (2013): 742–747, https://doi.org/10.1038/nnano.2013.176.

6. S. Parkin and S.-H. Yang, "Memory on the Racetrack," *Nature Nanotechnology* 10 (2015): 195–198.

7. G. Gubbiotti, A. Barman, S. Ladak, et al., "Roadmap on 3D Nano-Magnetism," *Journal of Physics-Condensed Matter* 37 (2025): 143502.

8. Y. Zhou, "Magnetic Skyrmions: Intriguing Physics and New Spintronic Device Concepts," *National Science Review* 6 (2019): 210–212, https://doi.org/10.1093/nsr/nwy109.

9. J. Grollier, D. Querlioz, K. Camsari, K. Everschor-Sitte, S. Fukami, and M. Stiles, "Neuromorphic Spintronics," *Nature Electronics* 3 (2020): 360–370, https://doi.org/10.1038/s41928-019-0360-9.

10. C. H. Marrows, J. Barker, T. A. Moore, and T. Moorsom, "Neuromorphic Computing With Spintronics," *npj Spintronics* 2 (2024): 12, https://doi.org/10.1038/s44306-024-00019-2.

11. G. Tanaka, T. Yamane, J. B. Héroux, et al., "Recent Advances in Physical Reservoir Computing: A Review," *Neural Networks* 115 (2019): 100–123, https://doi.org/10.1016/j.neunet.2019.03.005.

12. K. Raab, M. A. Brems, G. Beneke, et al., "Brownian Reservoir Computing Realized Using Geometrically Confined Skyrmion Dynamics," *Nature Communications* 13 (2022): 6982, https://doi.org/10.1038/s41467-022-34309-2.

13. T. Yokouchi, S. Sugimoto, B. Rana, et al., "Pattern Recognition With Neuromorphic Computing Using Magnetic Field–Induced Dynamics of Skyrmions," *Science Advances* 8 (2022): abq5652, https://doi.org/10.1126/sciadv.abq5652.

14. O. Lee, T. Wei, K. D. Stenning, et al., "Task-Adaptive Physical Reservoir Computing," *Nature Materials* 23 (2024): 79–87.

15. M. Garst, J. Waizner, and D. Grundler, "Collective Spin Excitations of Helices and Magnetic Skyrmions: Review and Perspectives of Magnonics in Non-Centrosymmetric Magnets," *Journal of Physics D: Applied Physics* 50 (2017): 293002, https://doi.org/10.1088/1361-6463/aa7573.

16. A. Aqeel, J. Sahliger, T. Taniguchi, et al., "Microwave Spectroscopy of the Low-Temperature Skyrmion State in Cu_2OSeO_3," *Physical Review Letters* 126 (2021): 017202, https://doi.org/10.1103/PhysRevLett.126.017202.

17. W. Koshibae and N. Nagaosa, "Theory of Antiskyrmions in Magnets," *Nature Communications* 7 (2016): 10542, https://doi.org/10.1038/ncomms10542.

18. M. Hoffmann, B. Zimmermann, G. P. Muller, et al., "Antiskyrmions Stabilized at Interfaces by Anisotropic Dzyaloshinskii-Moriya Interactions," *Nature Communications* 8 (2017): 308, https://doi.org/10.1038/s41467-017-00313-0.

19. T. Ma, A. K. Sharma, R. Saha, et al., "Tunable Magnetic Antiskyrmion Size and Helical Period From Nanometers to Micrometers in a D_{2d} Heusler Compound," *Advanced Materials* 32 (2020): 2002043, https://doi.org/10.1002/adma.202002043.

20. J. Jena, B. Göbel, V. Kumar, I. Mertig, C. Felser, and S. Parkin, "Evolution and Competition Between Chiral Spin Textures in Nanostripes With D_{2d} Symmetry," *Science Advances* 6 (2020): abc0723, https://doi.org/10.1126/sciadv.abc0723.

21. J. Jena, S. Koraltan, F. Bruckner, et al., "Topological Phase Transformation and Collapse Dynamics of Spin Textures in a Non-Centrosymmetric D_{2d} System," *Advanced Functional Materials* 34 (2024): 2403358.

22. L. Camosi, N. Rougemaille, O. Fruchart, J. Vogel, and S. Rohart, "Micromagnetics of Antiskyrmions in Ultrathin Films," *Physical Review B* 97 (2018): 134404, https://doi.org/10.1103/PhysRevB.97.134404.

23. Z. Cheng, H. Chen, S. Huang, and Y. Wu, "Spin Wave Mode Coupling in Antiskyrmions Induced by Rotational Symmetry Breaking," *Physical Review B* 109 (2024): 104431, https://doi.org/10.1103/PhysRevB.109.104431.

24. L. Peng, R. Takagi, W. Koshibae, et al., "Controlled Transformation of Skyrmions and Antiskyrmions in a Non-Centrosymmetric Magnet," *Nature Nanotechnology* 15 (2020): 181–186, https://doi.org/10.1038/s41565-019-0616-6.

25. W. Hu, Z. Zhang, Y. Liao, et al., "Distinguishing Artificial Spin Ice States Using Magnetoresistance Effect for Neuromorphic Computing," *Nature Communications* 14 (2023): 2562, https://doi.org/10.1038/s41467-023-38286-y.

26. K. Karube, J. White, N. Reynolds, et al., "Robust Metastable Skyrmions and Their Triangular–Square Lattice Structural Transition in a High-Temperature Chiral Magnet," *Nature Materials* 15 (2016): 1237–1242, https://doi.org/10.1038/nmat4752.

27. T. Nakajima, H. Oike, A. Kikkawa, et al., "Skyrmion Lattice Structural Transition in MnSi," *Science Advances* 3 (2017): 1602562, https://doi.org/10.1126/sciadv.1602562.

28. R. Takagi, Y. Yamasaki, T. Yokouchi, et al., "Particle-Size Dependent Structural Transformation of Skyrmion Lattice," *Nature Communications* 11 (2020): 5685, https://doi.org/10.1038/s41467-020-19480-8.

29. P. Vir, N. Kumar, H. Borrmann, et al., "Tetragonal Superstructure of the Antiskyrmion Hosting Heusler Compound $Mn_{1.4}PtSn$," *Chemistry of Materials* 31 (2019): 5876–5880, https://doi.org/10.1021/acs.chemmater.9b02013.

30. Z. He, Z. Li, Z. Chen, et al., "Experimental Observation of Current-Driven Antiskyrmion Sliding in Stripe Domains," *Nature Materials* 23 (2024): 1048–1054, https://doi.org/10.1038/s41563-024-01870-8.

31. K. Ishizuka and B. Allman, "Phase Measurement of Atomic Resolution Image Using Transport of Intensity Equation," *Journal of Electron Microscopy* 54 (2005): 191–197.

32. K. Shibata, A. Kovács, N. Kiselev, N. Kanazawa, R. Dunin-Borkowski, and Y. Tokura, "Temperature and Magnetic Field Dependence of the Internal and Lattice Structures of Skyrmions by Off-Axis Electron Holography," *Physical Review Letters* 118 (2017): 087202, https://doi.org/10.1103/PhysRevLett.118.087202.

33. N. Romming, A. Kubetzka, C. Hanneken, K. von Bergmann, and R. Wiesendanger, "Field-Dependent Size and Shape of Single Magnetic Skyrmions," *Physical Review Letters* 114 (2015): 177203, https://doi.org/10.1103/PhysRevLett.114.177203.

34. U. K. Rößler, A. A. Leonov, and A. N. Bogdanov, "Chiral Skyrmionic Matter in Non-Centrosymmetric Magnets," *Journal of Physics: Conference Series* 303 (2011): 012105.

35. J.-S. B. Tai and I. I. Smalyukh, "Three-Dimensional Crystals of Adaptive Knots," *Science* 365 (2019): 1449–1453, https://doi.org/10.1126/science.aay1638.

36. A. Vansteenkiste, J. Leliaert, M. Dvornik, M. Helsen, F. Garcia-Sanchez, and B. Van Waeyenberge, "The Design and Verification of MuMax3," *AIP Advances* 4 (2014): 107133, https://doi.org/10.1063/1.4899186.

37. S.-Z. Lin, A. Saxena, and C. D. Batista, "Skyrmion Fractionalization and Merons in Chiral Magnets With Easy-Plane Anisotropy," *Physical Review B* 91 (2015): 224407, https://doi.org/10.1103/PhysRevB.91.224407.

38. X. Wan, Y. Hu, and B. Wang, "Exchange-Anisotropy-Induced Intrinsic Distortion, Structural Transition, and Rotational Transition in Skyrmion Crystals," *Physical Review B* 98 (2018): 174427, https://doi.org/10.1103/PhysRevB.98.174427.

39. T. Schulz, R. Ritz, A. Bauer, et al., "Emergent Electrodynamics of Skyrmions in a Chiral Magnet," *Nature Physics* 8 (2012): 301–304, https://doi.org/10.1038/nphys2231.

40. C. Hanneken, F. Otte, A. Kubetzka, et al., "Electrical Detection of Magnetic Skyrmions by Tunnelling Non-Collinear Magnetoresistance," *Nature Nanotechnology* 10 (2015): 1039–1042, https://doi.org/10.1038/nnano.2015.218.

41. X. Zhang, Y. Zhou, K. M. Song, et al., "Skyrmion-Electronics: Writing, Deleting, Reading and Processing Magnetic Skyrmions Toward Spintronic Applications," *Journal of Physics-Condensed Matter* 32 (2020): 143001.

42. R. Streubel, "Phase Contrast Imaging of Non-Collinear Spin Textures With Lorentz Microscopy," *Journal of Materials Research* 38 (2023): 4977–4994, https://doi.org/10.1557/s43578-023-01216-1.

43. F. Zheng, F. N. Rybakov, N. S. Kiselev, et al., "Magnetic Skyrmion Braids," *Nature Communications* 12 (2021): 5316, https://doi.org/10.1038/s41467-021-25389-7.

Supporting Information

Additional supporting information can be found online in the Supporting Information section.

Supporting File: adfm74588-sup-0001-SuppMat.pdf.